Ambient noise surface wave tomography to determine the shallow shear velocity structure at Valhall: depth inversion with a Neighbourhood Algorithm

A. Mordret, M. Landès, N. M Shapiro, S. Singh, Philippe Roux

Geophysical Journal International

Geophys. J. Int. (2014) **198,** 1514–1525 doi: 10.1093/gji/ggu217
GJI Seismology

Ambient noise surface wave tomography to determine the shallow shear velocity structure at Valhall: depth inversion with a Neighbourhood Algorithm

A. Mordret,[1] M. Landès,[1] N. M. Shapiro,[1] S. C. Singh[2] and P. Roux[3]

[1]*Equipe de Sismologie, Institut de Physique du Globe de Paris, Sorbonne Paris Cité, Université Paris Diderot, CNRS (UMR* 7154*),* 1 *rue Jussieu, F-*75005 *Paris, France. E-mail: mordret@ipgp.fr*
[2]*Laboratoire de Geoscience Marine, Institut de Physique du Globe de Paris, Sorbonne Paris Cité, Université Paris Diderot, CNRS (UMR* 7154*),* 1 *rue Jussieu, F-*75005 *Paris, France*
[3]*Institut des Sciences de la Terre, Université Joseph Fourier, CNRS UMR* 5275, *Maison des Géosciences,* 1381 *Rue de la Piscine, F-*38400 *Saint Martin d'Hères, France*

Accepted 2014 June 5. Received 2014 May 23; in original form 2014 February 10

SUMMARY

This study presents a depth inversion of Scholte wave group and phase velocity maps obtained from cross-correlation of 6.5 hr of noise data from the Valhall Life of Field Seismic network. More than 2 600 000 vertical–vertical component cross-correlations are computed from the 2320 available sensors, turning each sensor into a virtual source emitting Scholte waves. We used a traditional straight-ray surface wave tomography to compute the group velocity map. The phase velocity maps have been computed using the Eikonal tomography method. The inversion of these maps in depth are done with the Neighbourhood Algorithm. To reduce the number of free parameters to invert, geological *a priori* information are used to propose a power-law 1-D velocity profile parametrization extended with a gaussian high-velocity layer where needed. These parametrizations allowed us to create a high-resolution 3-D *S*-wave model of the first 600 m of the Valhall subsurface and to precise the locations of geological structures at depth. These results would have important implication for shear wave statics and monitoring of seafloor subsidence due to oil extraction. The 3-D model could also be a good candidate for a starting model used in full-waveform inversions.

Key words: Tomography; Surface waves and free oscillations; Seismic tomography.

1 INTRODUCTION

Seismic surface waves extracted from correlations of ambient noise are used in many geophysical applications to characterize the shallow subsurface (e.g. Campillo *et al.* 2011; Ritzwoller *et al.* 2011). Depending on the target studied, the scale of the tomographies based on surface waves can range from several thousands of kilometres with penetration depth down to the transition zone (e.g. Kustowski *et al.* 2008; Nishida *et al.* 2009), to metre scale for geotechnics and near-surface characterization applications (e.g. Xia *et al.* 1999). However, there are very few studies which investigate the depth ranges between several tens of metres to several hundreds of metres (down to 1 km) using surface waves. Until recently, only the spatial autocorrelation of microtremors method (Aki 1957; Okada & Suto 2003) was able to reach 100 m depth (e.g. Wathelet *et al.* 2005). The main cause of this lack of intermediate-depth studies is the lack of intermediate-frequency surface wave measurements. Indeed, in a vertically heterogeneous medium, surface waves are dispersive because waves at different frequencies sample different depths and, therefore, travel with different speed. Most of the surface waves energy travels within one wavelength from the surface, thus, to investigate depth down to 1 km, one needs surface waves with wavelength smaller than 1 km, that is frequencies between ∼0.5 and 2 Hz for phase velocities below 1000 m s^{-1}. These frequencies are too low to be generated with most of existing types of active sources. On the other hand, the surfaces waves at such short periods are quickly attenuated and are not present in records from distant earthquakes.

Seismic noise at high frequency, part of the secondary microseismic peak (Longuet-Higgins 1950; Herbers & Guza 1994) may be used to fill this 'gap' in surface wave measurements. Recently, it has been shown that the seismic noise could be used to image the crust (e.g. Shapiro *et al.* 2005). The principle is based on the fact that the cross-correlation (CC) of the seismic noise recorded at two sensors is an approximation of the surface wave part of the Green's function of the media between the sensors (e.g. Campillo 2006; Gouédard *et al.* 2008). Since then, many regional scale studies has been performed and showed unprecedented high-resolution images of the crust and the uppermost mantle (e.g. Lin *et al.* 2007; Moschetti *et al.* 2007; Yang *et al.* 2007; Lin *et al.* 2008; Zheng *et al.* 2008; Stehly *et al.* 2009; Zheng *et al.* 2011). These studies strongly highlight the complementarity between the frequency content of the seismic noise and the earthquakes. Some of them compute

hybrid dispersion curves with the high-frequency part from the noise and the low-frequency part from earthquake data (e.g. Yao *et al.* 2006; Yang *et al.* 2008). Most of ambient noise tomography studies focused on relatively large scales with periods between 5 and 50 s. At smaller scale, ambient noise tomography has been used to image volcanic edifices at periods between 1 and 10 s (Brenguier *et al.* 2007; Masterlark *et al.* 2010; Stankiewicz *et al.* 2010; Luzón *et al.* 2011), sedimentary basin at periods between 0.5 and 3 s (e.g. Huang *et al.* 2010), geothermal areas between 3 and 10 s (Yang *et al.* 2011) or 1 and 5 s (Calò *et al.* 2013) and landslides (Renalier *et al.* 2010) at periods between 1.7 and 5 Hz.

In marine environment, the sediments of the upper layers of the seafloor are saturated with water and the shear wave velocity may be very low. Hamilton (1976) gave a seminal review on shear wave properties in shallow marine sediments and brought an empirical law for *S*-wave versus depth in sandy sediments that has been widely used in the literature (e.g. Gabriels *et al.* 1987; Mooney *et al.* 1998; Buckingham 2000, 2005; Rodriguez-Suarez & Stewart 2000): $V_s = 128\, d^{0.28}$, where V_s is the shear wave velocity in m s^{-1} and d the depth in m. In this configuration, one can expect wavelengths of the order of 1 km and smaller at frequencies around 1 Hz and below, ideal to investigate the first hundreds of metres of the subsurface.

Bussat & Kugler (2011) were the first to propose a 3-D *S*-wave model of the first kilometre (and beyond) of a small seafloor portion (6 × 8 km) using ambient seismic noise records from ocean-bottom seismometres at 126 locations between 0.1 and 0.7 Hz. In this study, we use seismic noise records from the Valhall Life of the Field Seismic (LoFS) network to compute a high-resolution 3-D *S*-wave model of the Valhall field overburden down to 600 m. Previous results of group-velocity maps and phase-velocity maps from Mordret *et al.* (2013a,c), respectively, are used to perform the depth inversion.

After presenting the data and reminding the methods of ambient noise surface wave tomography, the description of the principles of dispersion curves inversion at depth using the Neighbourhood Algorithm (NA; Sambridge 1999) will be done in Section 2. Then, the application of this method to estimate an average 1-D *S*-wave velocity model for the whole area will be performed (Section 3). Section 4 will present the construction of the 3-D model. Finally, in Section 5 the results will be discussed in the light of previous studies on the Valhall shallow overburden.

2 DATA AND METHODS

2.1 The Valhall LoFS data set

The Valhall LoFS network is a permanent ocean-bottom cables array made of 2320 four-component sensors (a three-component geophone and a hydrophone) installed on the seafloor of the North Sea, above the Valhall oil-field reservoir (VanGestel *et al.* 2008, Fig. 1). The dataset used in this study is made of 6.5 hr of continuous ambient seismic noise records and the computation of the CCs between every pair of sensors follows the method described by Mordret *et al.* (2013a). Between 0.5 and 2 Hz, the noise records are dominated by the natural secondary microseism and the noise source distribution is fairly isotropic. This results in emergence of dispersive Scholte waves from the vertical–vertical (ZZ) component CCs.

2.2 Ambient noise surface wave tomography

The surface wave tomography is done using a common three-strep approach (e.g. Ritzwoller *et al.* 2011). First, frequency-dependent

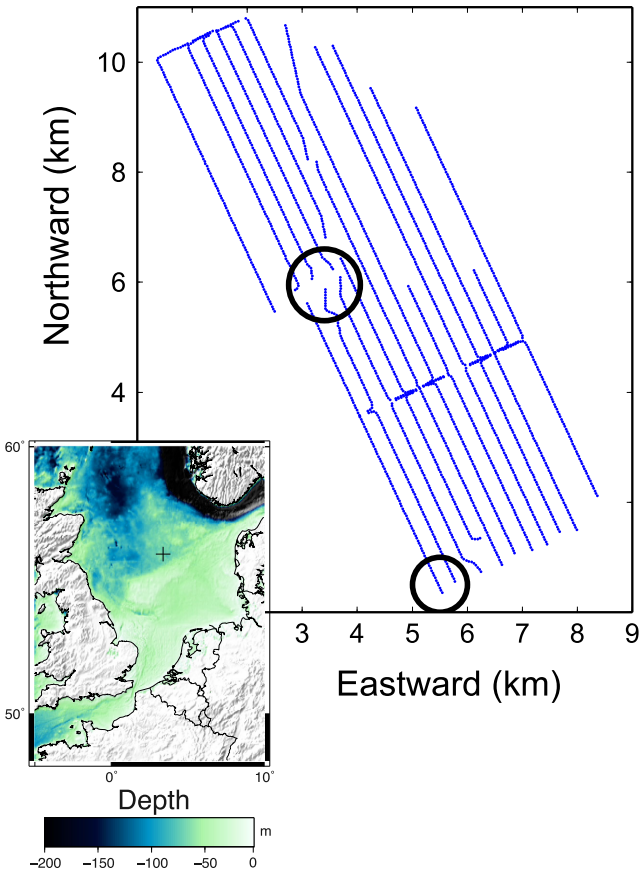

Figure 1. Map of the Valhall *LoFS* array. Each blue point represents a 4C sensor. The black circles show the approximate positions of the exploitation platforms. The insets show the geographical location of the Valhall field with the black cross showing the location of the Valhall LoFS array. The bathymetry is shown as the background of the right inset.

group and/or phase traveltimes are measured from every inter-station noise CC. This procedure can be done for instance, using the Frequency-Time Analysis technique of Levshin *et al.* (1989). In the second step, the surface wave traveltimes are inverted to construct 2-D phase and group velocity maps at different frequencies. This is done with surface wave tomography algorithms (e.g. Barmin *et al.* 2001; Ekström 2011) for group velocities and with the eikonal tomography (Lin *et al.* 2009) for the phase velocities. Construction of the Sholte-wave surface wave dispersion maps at Valhall is described by Mordret *et al.* (2013a,c). The final step is to invert the dispersion maps for the depth structure. This inversion is performed in every cell of the geographical grid where local regionalized dispersion curves are inverted for a local 1-D shear velocity model. Combining all 1-D profiles from all cells, result in the final 3-D model of the subsurface. At Valhall, the grid used has 231 × 181 cells with 50 m bins size.

2.3 Depth inversion using the NA

In order to invert at depth the group and phase velocity maps, the NA developed by Sambridge (1999) has been chosen. The NA is a Monte-Carlo global direct-search technique developed to efficiently sample a model-space. A model is a set of different parameters and the model-space associated has the same dimension as the number of parameters used to describe a model. The model-space is bounded by *a priori* minimum and maximum values for each parameter. In the case of local dispersion curves inversion, the model is a 1-D

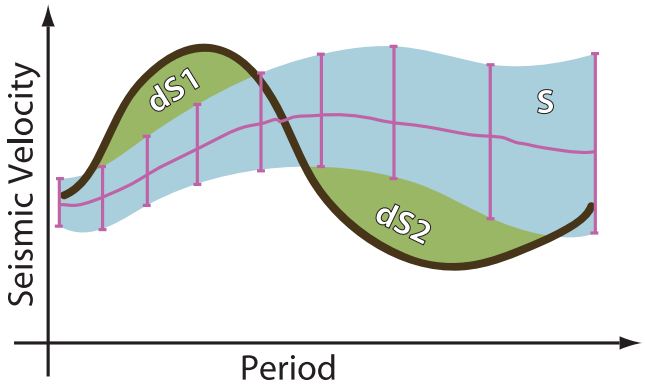

Figure 2. Illustration of the misfit computation between a theoretical dispersion curve in brown and a measured dispersion curve with its uncertainties in pink. In this example, the misfit is the normalised area $(dS1 + dS2)/S$.

layered *S*-wave depth/velocity profile and the parameters can be, for instance, the thickness and the velocity of each layer. Because of the weaker sensitivity of surface waves to *P*-wave velocities and densities, these quantities are not considered as free parameters and are related to V_S via an empirical relation: $V_P = 1.16V_S + 1.36$ (Castagna *et al.* 1985) and $\rho(\mathrm{g\,cm^{-3}}) = 1.74V_P^{0.25}$ with V_P in $\mathrm{km\,s^{-1}}$ (Brocher 2005) . We do not take into account the dispersion caused by the attenuation structure. The description of the parametrization chosen for this study can be found in Section 2.4.

For a single inversion, the NA is made of different steps. In a first step, the NA generates n_1 models (i.e. n_1 1-D layered *S*-wave velocity profiles) randomly distributed inside the model-space. Then, a mesh of Voronoi cells (the nearest neighbour portion of space associated with each model) is created. For each model, a theoretical dispersion curve is computed using routines from Herrmann & Ammon (2004) and the misfit between the theoretical and the observed dispersion curve is assigned to the corresponding cell. As shown in Fig. 2, the misfit between the measured dispersion curve and the theoretical one is the area of the theoretical dispersion curve outside the area defined by the measured dispersion curve and its uncertainties, normalized by the area of the measured dispersion curve. In the example of Fig. 2, the misfit would be $(dS1 + dS2)/S$. We choose this misfit definition to avoid to over-fit the dispersion curves. Given the uncertainties of the dispersion curve picking and of the surface wave tomography method, it is sufficient to fit the dispersion curves within one standard deviation of the data.

In a second step, the best n_c cells (i.e. with the lowest misfit) are chosen and n_s new models are generated within each of these cells. A new set of Voronoi cells is generated taking account of every model (the previous and the new ones). The new misfits are computed and the best n_c cells are chosen to be re-sampled. This last procedure is repeated and the algorithm stops after n_i iterations. The main advantage of this algorithm is to focus simultaneously on the most promising zones of the model-space and to rapidly converge to the global minimum while keeping in memory the high-misfit models information. At the end of the process the model-space has been fully explored and one can have a good estimation of the misfit-function 'topography'.

2.4 Parametrization

As mentioned above, in the local dispersion curve inversion problem, the model is usually a 1-D layered *S*-wave velocity profile where the parameters are the thickness and the velocity in each layer. The drawback of this parametrization is that one has to invert for $2n_l$ parameters where n_l is the number of layers. If n_l is chosen too large, the volume of the model-space becomes immense and it is very time-consuming to sample it densely enough. Moreover, as the number of parameters grows, the non-unicity of the solution becomes more and more significant, that is the number of valleys in the misfit-function 'topography' increases and it may be difficult to chose the right model which has a physical/geological meaning. *A priori* physical constraints on the properties of the subsurface help to circumvent the non-unicity of the surface wave inversion (e.g. Shapiro & Ritzwoller 2004; Shapiro *et al.* 2004).

The structure of the Valhall field subsurface is well know from well logging as well as active seismic data (see Barkved 2012, for a review of the Valhall field monitoring techniques and a complete field description). Of particular interest is the full waveform inversion (FWI) done by Sirgue *et al.* (2010) which gave a 3-D *P*-wave velocity model of the complete field with an unprecedented resolution. Using these data and stratigraphic logs (Munns 1985), allows the simplification of the parametrization. At Valhall, the shallow subsurface is made of unconsolidated quaternary sediments for the first 600 m. At this depth, there is a structural discontinuity: the Pliocene-Pleistocene transition which separates the unconsolidated sediment from much harder tertiary shales with higher velocity. As shown by Hamilton (1976), the shear wave velocity profile with depth for compacting unconsolidated sediments can be modelled as a power-law (Wathelet *et al.* 2004):

$$V_s(d) = V_0\left((d+1)^{\alpha} - (d_0+1)^{\alpha} + 1\right), \quad (1)$$

where V_s is the *S*-wave velocity, d the depth, V_0 is the velocity at the seafloor, α is the power-law parameter and d_0 is the water depth. At Valhall, the bathymetry is very smooth and $d_0 = 70$ m is taken constant. In eq. (1), only V_0 and α are fitting parameters. Preliminary tests showed that the data required the presence of the Pliocene-Pleistocene transition as a high-velocity half-space at depth around 600 m and we chose to invert only for the velocity V_n of this half-space. The algorithm used for computing surface wave dispersion curves (Herrmann & Ammon 2004) requires describing the structure as a set of layers with constant elastic properties. Therefore, the shallow sediments are approximated with a set of 11 thin layers whose velocities are selected to fit eq. (1). This parametrization with only three parameters was sufficient to describe most of the data. However, in some places, a more complex parametrization has to be introduced to achieve a proper fit as described in Section 4.3.

3 AVERAGE *S*-WAVE VELOCITY MODEL

3.1 Measurement of average dispersion curves

Before inverting for the 3-D model, an inversion for the average 1-D model of the complete Valhall area is performed. To measure the average phase velocity dispersion curve the average CC gather is constructed by stacking every 2 690 040 ZZ correlations in 10-m interstation distance bins (Fig. 3). This stacking operation drastically increases the signal-to-noise ratio of the data and highlights different modes of the surface waves. This technique has recently been applied by Nishida (2013), Lin *et al.* (2013), Boué *et al.* (2013) to extract teleseismic propagation of body-waves contained in the seismic noise. In Fig. 3, the average correlations have been filtered between 0.1 and 6 Hz and an amplitude gain control has been applied. One can clearly observe the fundamental mode and the first overtone of the Scholte waves, whereas on single CC,

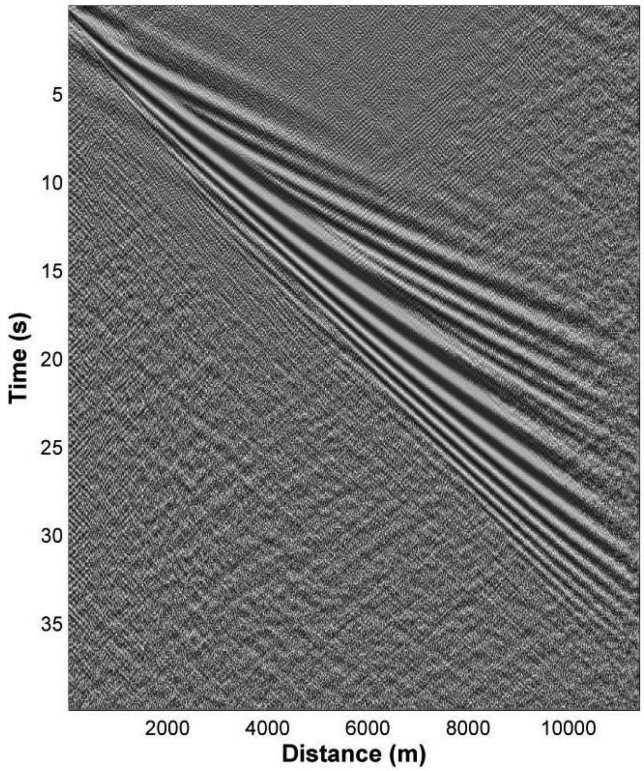

Figure 3. Average correlation gather. All 2 690 040 ZZ correlations are averaged in 10-m-interstation distance bins. An amplitude gain control has been applied to homogenize the amplitudes all along the gather. Note the strong dispersion and the different modes of the Scholte waves.

only the fundamental mode is visible. The frequency-wavenumber (F-K) analysis (Gabriels *et al.* 1987) of these records is performed to measure the dispersion curves associated to each mode (Fig. 4a). The F-K spectrum $U(k, f)$ of the gather $u(x, t)$ is given by

$$U(k,\, f) = \int_{-\infty}^{+\infty}\!\!\int u(x, t)\, \cdot\, e^{2i\pi(ft-kx)}\mathrm{d}x\,\mathrm{d}t, \qquad (2)$$

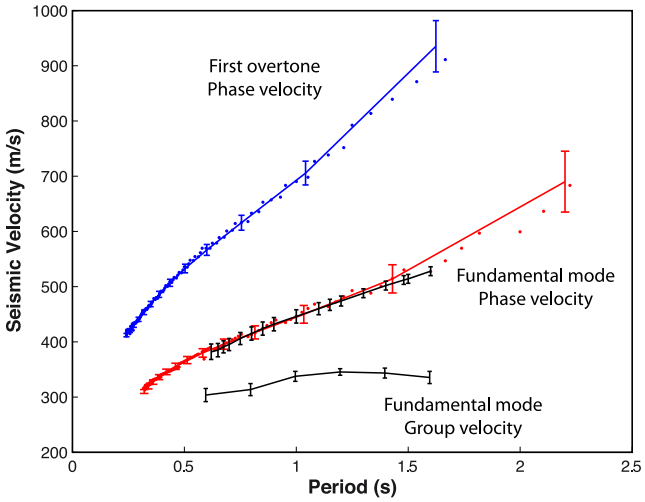

Figure 5. Average phase and group dispersion curves. The red and blue dots are the picks from Fig. 4 for the phase velocity fundamental mode and the first overtone, respectively. The red and blue curves with error-bars are the third-order polynomial fits to the picks. The black curves are the mean phase and group dispersion curves from the phase and group velocity maps (see the text for details).

where x the distance along the virtual array, t the time, k is the wavenumber in the x direction and f is the frequency. In the F-K domain, the dispersion curves are determined by picking the energy maxima. For every frequency f, a set of peaks $k_m(f)$ is obtained, where m is the mode number. The phase velocity dispersion curve is then

$$c_m(f) = \frac{f}{k_m(f)}\,. \qquad (3)$$

The red and blue dots in Fig. 4(b) show the picks made for the fundamental mode and the first overtone, respectively. Corresponding phase velocity dispersion curves are shown in Fig. 5. The red and the blue curves with the error-bars are the third-order polynomials used to fit the corresponding picks. As a comparison, the average phase velocity dispersion curve for the Valhall area is computed as the mean and standard deviation of the mean of the fundamental-mode phase velocity maps obtained by Mordret *et al.* (2013c) at

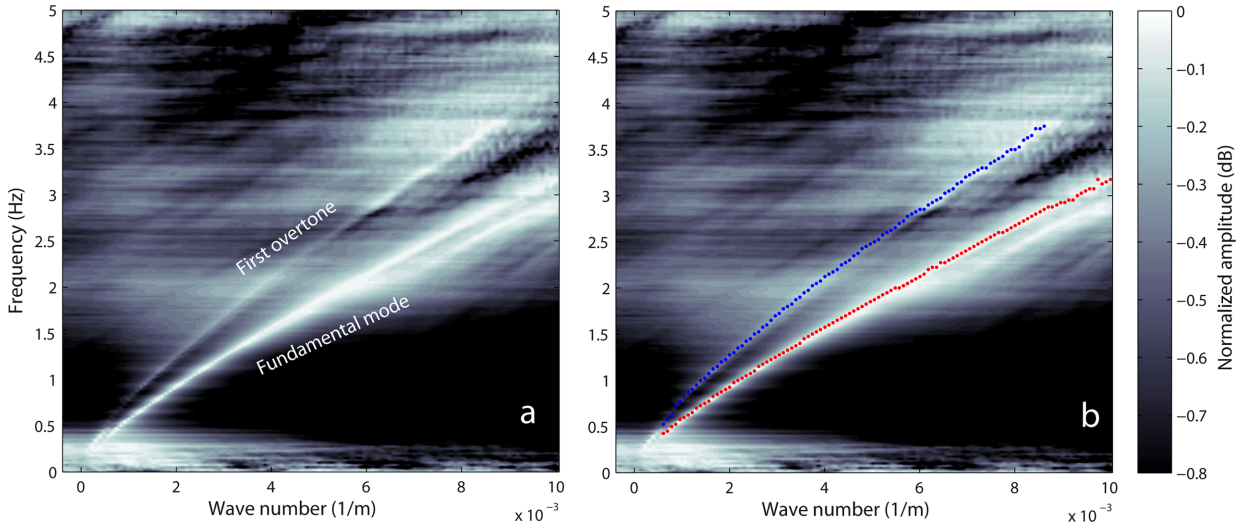

Figure 4. F-K analysis of the average correlation gather. (a) The raw diagram with the interpretation of the fundamental mode and the first overtone. (b) The picks of the fundamental mode and the first overtone dispersion curves are shown with red and blue dots, respectively.

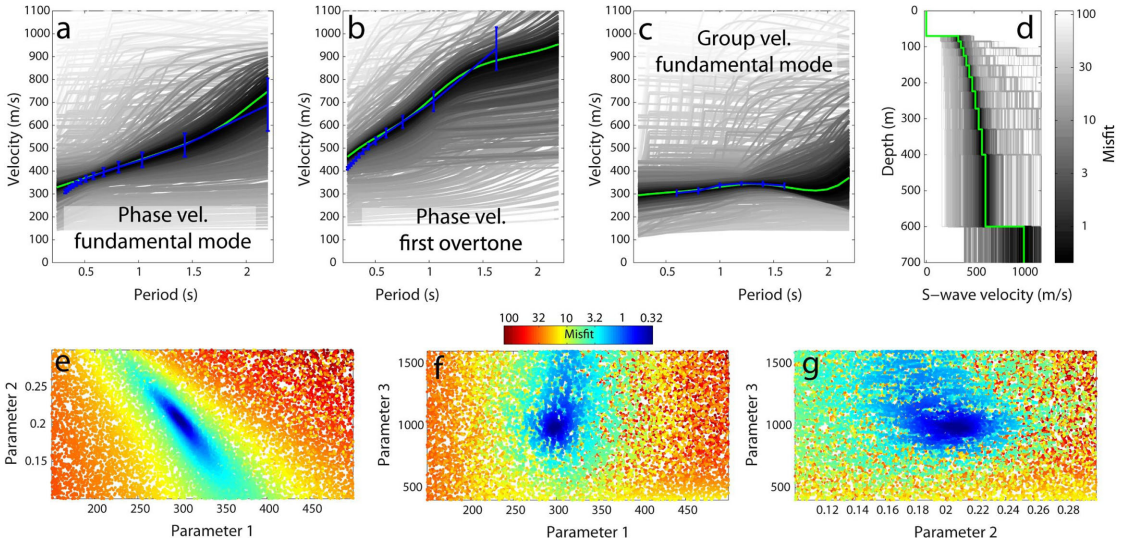

Figure 6. Inversion of average dispersion curves. (a)–(c) The dispersion curves associated with the models selected by the NA; the grey shade corresponds to the misfit value. The blue curves are the data and the green curves are the dispersion curves associated with the best-fit model. (d) The ensemble of different models tried by the NA; the thick green curve is the best-fit model. (e)–(g) The 2-D marginals of all couples of parameters. Parameter 1, 2 and 3 are V_0, α and V_n, respectively. Note the correlation between V_0 and α. The colour corresponds to the misfit value.

several frequencies. This curve and corresponding error-bars are shown with a black colour in Fig. 5. For the phase velocity fundamental mode, the two curves are very similar even though they are obtained with independent measurements. Fig. 5 also shows the average group velocity dispersion curve computed as the mean and standard deviation of the mean of the group velocity maps from Mordret *et al.* (2013a) that is used to constrain the inversion.

Two surface wave modes are present in our data and one may argue that there could be spurious events created by a non-optimal distribution of noise sources at the surface around the array and cross-terms correlation summation (Halliday & Curtis 2008). The mode that we interpret as the first overtone is only visible when stacking the tremendous number of correlation together (Figs 3–4). On single correlations, its energy is minimal and only the fundamental mode is dominant. Therefore, the cross-term summation should be weak. Moreover, even if we cannot locate precisely the noise sources, we know that they surround the array (Mordret *et al.* 2013a) and it is likely that they are spread all over the North-Sea seafloor and not confined in a narrow ring around the network. In this configuration, Kimman & Trampert (2010) showed that the correlations should be mostly free of spurious events.

3.2 Depth inversion of average dispersion curves

The power-law model with the three parameters V_0, α and V_n (described in Section 2.4) is used to invert for the average model. The bounds for the parameters are [150−500] m s^{-1} for V_0, [0.1−0.3] for α and [400−1600] m s^{-1} for V_n. The two velocity ranges are chosen considering the upper and lower-bounds of the dispersion curves as well as *a priori* knowledge from the Valhall field geology. The value range for α has to be between 0 and 1 to have a smoothly increasing velocity with depth and the final range is chosen by trial and errors. The NA was run with $n_1 = 10\,000$, $n_s = 1000$, $n_c = 5$ and $n_i = 8$ (see Section 2.3 for description). During this inversion 50 000 models have been tested. The best-fit solution and corresponding dispersion curves are shown with green lines in Fig. 6. The three best parameters are $V_0 = 297$ m s^{-1}, $\alpha = 0.208$ and $V_n = 983$ m s^{-1}. Figs 6(e–g) show the 2-D marginals associated with each couple of parameters. The topography of the misfit function is very smooth with a clear global minimum with a value around 0.4. Moreover, the parameters 1 and 2, that is V_0 and α are correlated. Fig. 7 shows the convergence of the three parameters as a function of the number of iteration. After seven iterations, the NA reached the final parameter values.

Beside a relatively poor fitting of the very short periods that would require a smaller velocity of the first layer, the power-law-parametrization assumption is sufficient to model accurately the average velocity profile of the first 600 m at the Valhall area. This average velocity structure is used as a reference model for the 3-D inversion.

4 3-D SHEAR VELOCITY MODEL

4.1 Inversion with a three-parameters model

In a first step, the 1-D local inversions are performed using the three-parameters-power-law model (Section 2.4) in every cell of the grid. In this inversion, the input data are the local fundamental-mode phase velocities dispersion curves at periods between 0.7 and 1.6 s (with 0.1 s steps) and the local fundamental-mode group velocities dispersion curves at periods between 0.6 and 1.6 s (with 0.2 s steps). The NA was run with $n_1 = 10\,000$, $n_s = 500$, $n_c = 5$ and $n_i = 5$ to test 25 000 models. The best-fit 1-D profile is kept for every cell. Fig. 8 shows the map of the best misfits. Most of the area exhibits reasonably low misfit (<1), indicating that the power-low approximation for the velocity profile at depth is a good model. However, in the south-eastern corner of the field, the misfits are anomalously high, demonstrating that the dispersion curves from this area cannot be fitted with a power-law model, as shown in Fig. 9. There is a large palaeochannel in this area at a depth about 200–250 m that is clearly visible as a very high-velocity anomaly in the FWI *P*-wave model of Sirgue *et al.* (2010). With such a large high-velocity body at depth, the parametrization has to be modified to take it into account in the inversion.

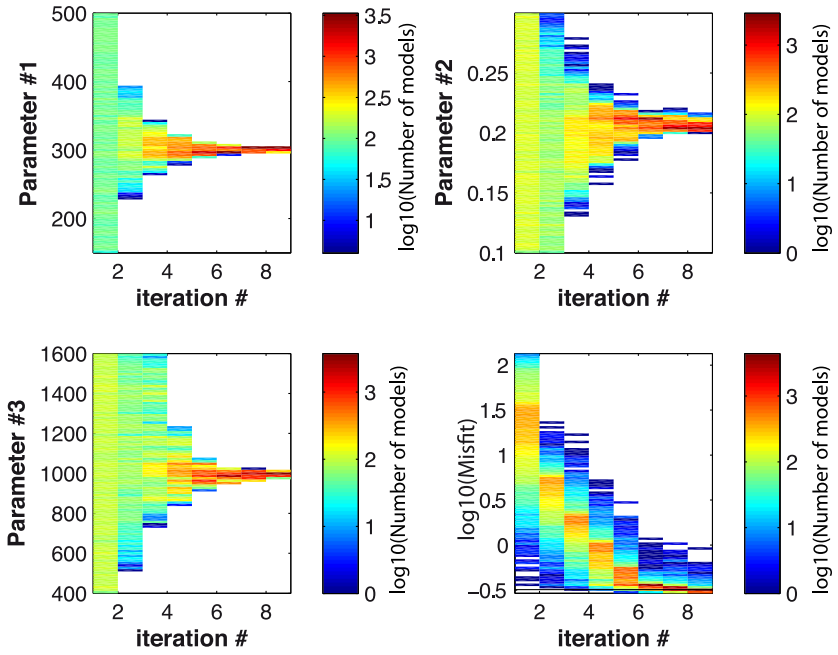

Figure 7. Convergence of the average model parameters with respect to the number of iterations of the NA. The lower right-hand panel shows the evolution of the misfit during the inversion. After seven iterations all three parameters have converged and the misfit does not evolve any more. The colour shows the number of model for each parameter and each iteration.

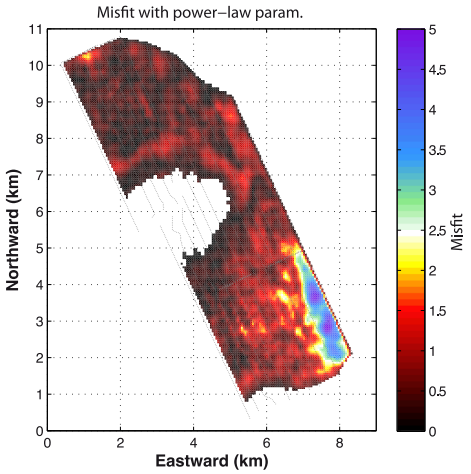

Figure 8. Map of the minimum misfit from the inversion with the 'power law' parametrization at each cell. Note that the misfits are low at most of the locations except in the south-eastern corner of the field where there is a large palaeochannel at depth.

4.2 Modified parametrization for the palaeochannel region

First, the average dispersion curves for the region where the palaeochannel is located is computed. The contour of misfit = 2 (Fig. 8) is used as the limit of this region and averaged phase and group velocities are computed for this area. These dispersion curves are then inverted with a parametrization consisting on the same power-law as eq. (1) to which a Gaussian-bell curve with varying depth, width and height to model an anomalous deep velocity layer is added:

$$V_s(d) = V_0\left((d+1)^{\alpha} - (d_0+1)^{\alpha} + 1\right) + \Delta V_l\, e^{\frac{(d-d_l)^2}{2\sigma_l^2}}. \qquad (4)$$

This parametrization requires three more parameters: ΔV_l, the velocity perturbation in the layer (can be positive or negative), d_l, the depth of the layer and σ_l the thickness of the layer. After inversion of 61 000 models with the NA parameters $n_1 = 25\,000$, $n_s = 2000$, $n_c = 3$ and $n_i = 6$, the best average model for the palaeochannel region was $V_0 = 276\,\mathrm{m\,s^{-1}}$, $\alpha = 0.22$, $V_n = 1077\,\mathrm{m\,s^{-1}}$, $\Delta V_l = 140\,\mathrm{m\,s^{-1}}$, $d_l = 186\,\mathrm{m}$ and $\sigma_l = 89\,\mathrm{m}$. These values are in good agreement with the values from the FWI of (Sirgue *et al.* 2010) in term of depth, velocity anomaly and thickness. Fig. 10 compares the global average model in blue using the 'power law' parametrization (already shown in Fig. 6c) with the best average palaeochannel model using parameters above.

To proceed with the local inversion in every grid cell, the parametrization is simplified by fixing the depth and the thickness of the palaeochannel layer (d_l and σ_l) to values from the average palaeochannel model. Therefore, the final parametrization includes four parameters: V_0, α, V_n and ΔV_l. We chose the sparsest parametrization which allows the misfit anomaly in Fig. 8 to be corrected. A six parameters inversion may have allowed us to extract a palaeochannel model closer to reality but with a risk of overparametrization. The four parameters model may be not the best model but it is a sufficient one to explain most of the observed dispersion.

4.3 Construction of a hybrid model

Adding a single additional parameter into the inversion helps to improve the fit to the data in the palaeochannel region. However, in most of the locations outside this region, the more complex parametrization does not really improve the misfit and adding the fourth parameter, the 'Gaussian layer' could result in less stable inversion results. Therefore, a final hybrid 3-D model is constructed only using the results form the 'Gaussian layer' parametrization in locations where an additional model parameter results in statistically significant improvement of the misfit. In all other locations, the

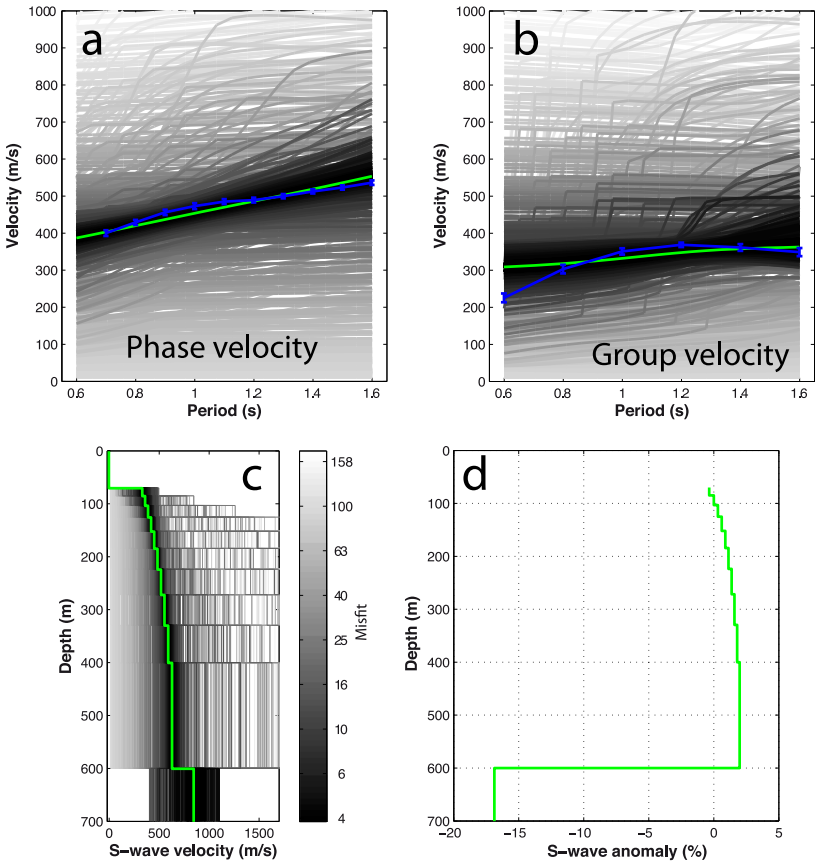

Figure 9. Results of the local inversion at a point located 7.5 km eastward, 3 km northward at the location of a large palaeochannel at depth (same point as the one shown in Fig. 13c). Both phase and group velocity dispersion curves [(a) and (b), respectively] cannot be fitted. Frame (c) shows the ensemble of models as well as the best-fit one (in green) and frame (d) shows the *S*-wave anomaly of the best model with respect to the average model.

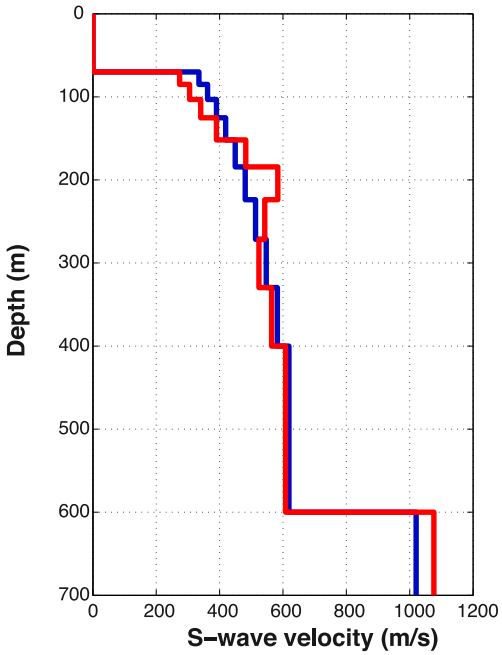

Figure 10. Global average model using 'power law' parametrization (blue profile) and best average model for the large palaeochannel region using a 'power law plus Gaussian layer' parametrization (red profile).

results obtained with the more simple 'power law' parametrization are kept. A *F*-test is performed to assess this question (see, e.g. Stein & Gordon 1984; Trampert & Spetzler 2006; Pollitz & Snoke 2010, for *F*-test applications in geoscience).

If a set of N data (combined number of discrete frequencies where phase and group velocities were measured) is fitted with two models with p and q parameters and $q > p$, the second model should fit the data better. The test uses the evaluation of the χ^2 between the data and the models as the sum of the squares of the differences between the data, d, and model predictions , d^m, normalized by the variance of data (the error-bars of the dispersion curves), σ^2:

$$\chi^2 = \sum_{i=1}^{N} \frac{(d_i - d_i^m)^2}{\sigma_i^2}. \quad (5)$$

In principle, $\chi^2(q)$ should be less than $\chi^2(p)$. To test if this reduction is significant, the following statistic is used:

$$F = \frac{[\chi^2(p) - \chi^2(q)]/(q-p)}{\chi^2(q)/(N-q)}. \quad (6)$$

The function F is F-distributed with $\nu_1 = q - p$ and $\nu_2 = N - q$ degrees of freedom. The test examines the probability $P_f(F, \nu_1, \nu_2)$ of observing an F value greater than the observed value F for a random sample with ν_1 and ν_2 degrees of freedom. Thus, for example, if P_f is 0.01, there is only a 1 per cent risk that the improvement in fit is due purely to chance.

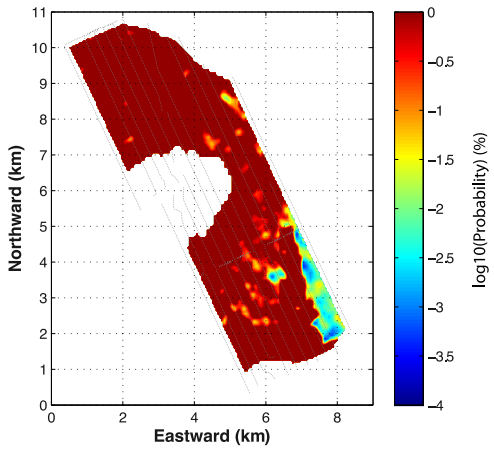

Figure 11. Result of the *F*-test comparing the 'Power law' parametrization with the 'Gaussian layer' parametrization. The probabilities are smaller than 1 per cent in the palaeochannel region, showing that the 'Gaussian-layer' parametrization significantly improved the fit to the data in this area.

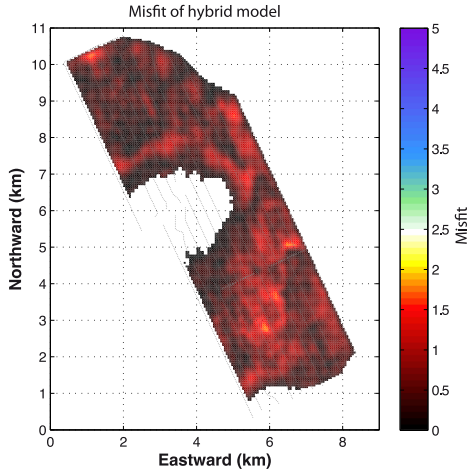

Figure 12. Map of the minimum misfit for the 'hybrid' model that is constructed with using the 'Gaussian layer' parametrization in the palaeochannel region and the 'power law' parametrization elsewhere.

In this study, the comparison is done on the inversion without or with a Gaussian anomalous velocity layer. In the first case, the data are $N = 16$-points dispersion curves fitted with $p = 3$ parameters, in the second they are fitted with $q = 4$ parameters. Fig. 11 shows for each cell the probability $P_f(F, \nu_1, \nu_2)$ that the misfit reduction is due to chance. At most of the cells in the palaeochannel area the probability is smaller than 1 per cent meaning that there is more than 99 per cent of probability that the supplementary parameter introduced by the Gaussian layer brought significantly more information than the simple power-law parametrization. It has to be noted that this area where the probability is the lowest corresponds to the cells used to compute the palaeochannel average dispersion curve.

The final 3-D model is then constructed by merging results of the inversion with the 'Gaussian layer' parametrization in the palaeochannel region where it significantly improved the misfit with the results of the 'power law' parametrization elsewhere. Fig. 12 shows the misfit map of the 'hybrid' model. The new parametrization removed completely the misfit anomaly shown in Fig. 8.

Fig. 13 shows three examples of local inversion at three particular locations. In the panel (a), the inversion is done with the power-law parametrization for a point which does not show any particular anomalies. This point has velocity profile with depth very comparable with the global average velocity model. The panel (b) shows the inversion done with the 'power-law model' at a point exhibiting a very low-velocity anomaly. Even for this anomalous structure, the power-law parametrization still holds. Finally, the panel (c) shows the inversion for the same point used in Fig. 9 with the 'Gaussian layer' parametrization. The fit is drastically improved and the palaeochannel shows a high-velocity anomaly which reaches 20 per cent, close to what is observed in the FWI results of (Sirgue *et al.* 2010). Our parametrization is made of a half-space below 600 m depth that was necessary to fit the average dispersion curves because they exhibit longer periods than the local dispersion curves. As shown by Figs 6(f and g), the velocity of the half-space is not well resolved, even with the longer periods of the average dispersion curves. Then even if we keep this parametrization for the local inversions, the velocity in the half-space is poorly resolved and we do not interpret and discuss this value in the following.

5 INVERSION RESULTS AND DISCUSSION

Fig. 13(d) shows a slice into the 3-D 'hybrid' velocity model at a depth of 150 m below sea level that summarizes main structural features revealed by this study. The non-unicity of the surface wave inversion has been addressed by taking into account *a priori* knowledge of the Valhall subsurface. This allowed the modelling of the velocity profiles by simple functions with few fitting parameters. The drawback of this approach could be the oversimplification of the problem leading to an oversmoothed model. For instance, the structures that have a well-defined depth in reality can be smeared along the vertical direction. The palaeochannels that can be seen on the 150-m-depth slice in Fig. 13(d) (highlighted in red) are actually confined in the 105–150-m-depth interval for the shallower one in the North, and in the 150–195-m-depth interval for the deeper one in the South of the network (Sirgue *et al.* 2010; de Ridder & Biondi 2013). The depth of the deep channel is relatively well retrieved with the 'Gaussian-layer' parametrization, as shown on the profile DD′ (Fig. 14). At the same time, the image of the shallow channels (Fig. 14, profile AA′) extends to the seabed where it should not be. Improving vertical resolution in this very shallow part of the model would require measurements at higher frequencies (e.g. Mordret *et al.* 2013a). Such additional information could make possible introducing more refined parametrizations than a simple power low used in the present study. The final 3-D model is made of the aggregation of the best-fitting model at each location. However, to assess the uncertainties on the velocity values we obtained we measured the standard deviation of the velocity of the 1000 best-fitting models at each depth for every location. This results presented in the right-hand panels of Fig. 14 show that the velocity uncertainty is very small ($<5\,\mathrm{m\,s^{-1}}$) at most of the area and slightly increase in the palaeochannel zone where the four-parameters models were used. Overall, these absolute uncertainty values represent less than 5 per cent anomaly uncertainty. It has to be noted that the NA does not provide true probability distribution, which would need a resampling of the tested-model distribution. The values taken as the velocity uncertainty may underestimate the real uncertainties.

Despite its limited resolution in the vertical direction, the depth inversion permits to precise the location and shape of different geological structures previously highlighted by de Ridder & Dellinger (2011), Mordret *et al.* (2013a,c), de Ridder & Biondi (2013). Among them, two are of particular interest: the palaeochannels, and the

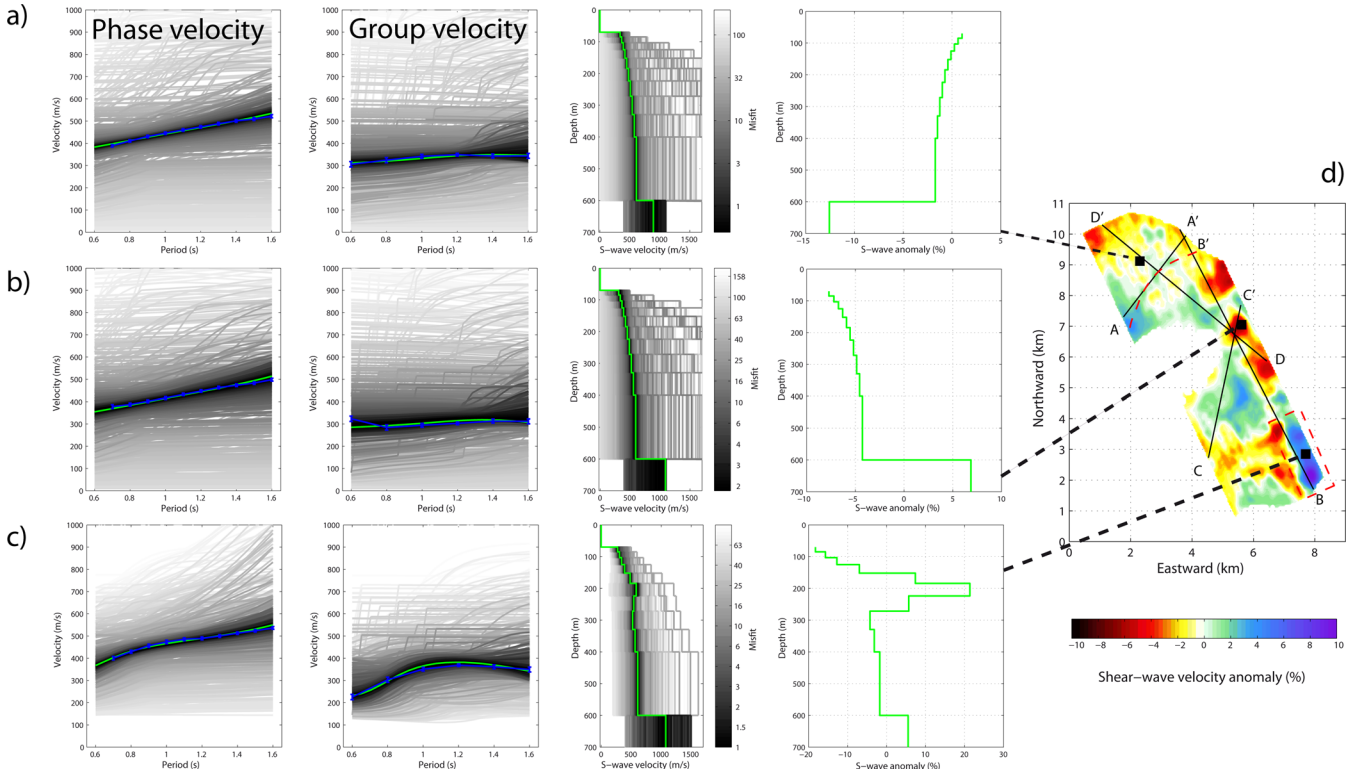

Figure 13. Examples of 1-D inversions at three locations. (a) Inversion with the 'power law' parametrization in a location where the velocity profile is similar to the average velocity model. The *S*-wave velocity misfit (right-hand panel) is close to zero at most of depths. (b) Inversion with the 'power law' parametrization in a location presenting a very low velocity anomaly. (c) Inversion with the 'Gaussian layer' parametrization in a location above the large palaeochannel (same point as Fig. 9). Note the drastic misfit improvement compared to Fig. 9. (d) Slice of the 'hybrid' 3-D shear-velocity model at 150 m depth below sea level. The thin black lines show the locations of the 2-D velocity profiles of Fig. 14. The red dashed lines highlight the palaeochannels.

shallow high-velocity and deep low-velocity anomalies at the centre of the array.

5.1 Geological structures

5.1.1 The palaeochannels

The palaeochannels present in the first 150 m of the subsurface below the seabed are well-known quaternary structures at Valhall. They were created at the end of the last ice age when the North Sea plateau emerged due to eustasy. Beside their geological interest, they have been good benchmark to assess the spatial resolution of the 3-D model obtained in this study. As mentioned before, the northern thin channel and the large southern one are not at the same depth, however, in the tomography there is a small depth range (around 150 m below sea level) where they overlap meaning that the inversion is not able to resolve features separated by less than 50 m in the vertical direction. The sections AA′ and BB′ in Fig. 14 are taken along the channels and illustrate this depth resolution. Fig. 15(a) shows the 3-D velocity anomaly iso-contour at 15 per cent highlighting the large palaeochannel. Both depth and lateral extent are well retrieved. This 15 per cent *S*-wave velocity anomaly is comparable to the velocity contrast obtained for *P*-wave velocity from FWI (Sirgue *et al.* 2010).

5.1.2 The reservoir subsidence effects

The second structure can be seen in Fig. 14, on the profiles CC′ and DD′ as a high-velocity anomaly in the shallow part of the model overlaying a low-velocity anomaly in the deeper part of the model. This particular configuration is the signature of the reservoir subsidence at depth (Barkved *et al.* 2005). Because of the production of the oil, the high-porosity chalk reservoir at about 2500 m depth is compacting leading to the subsidence of the whole overburden. The subsidence is varying along the rock-column above the reservoir with a stronger subsidence at the reservoir level (∼10 m) than at the surface (∼6 m, Kristiansen & Plischke 2010). This subsidence differential stretches the rocks in the overburden from ∼150 m down to the reservoir and the resulting volumetric strain decreases the seismic velocities (Barkved *et al.* 2005). Inversely, near the surface, the subsidence of the seafloor creates a bowl with a contractional regime in its centre leading to the increase of the seismic velocities (Barkved *et al.* 2005; Hatchell *et al.* 2009). Moreover, the edges of the bowl are in extension, opening concentric cracks which produce the concentric anisotropy pattern observed by, for example Barkved *et al.* (2005), Mordret *et al.* (2013b).

6 CONCLUSION

We inverted group and phase velocity maps obtained by ambient-noise surface wave tomography with the NA to construct a 3-D shear velocity model of the Valhall subsurface down to depth of 600 m. Only 6.5 hr of continuous vertical noise recorded at the Valhall LoFS network were necessary to compute the velocity maps at periods between 0.6 and 1.6 s. The parametrization of the inversion fitting a power-law or a power-law plus a Gaussian high-velocity layer to model the 1-D *S*-wave velocity profiles versus depth permitted to decrease the number of parameters to be inverted and reduced the

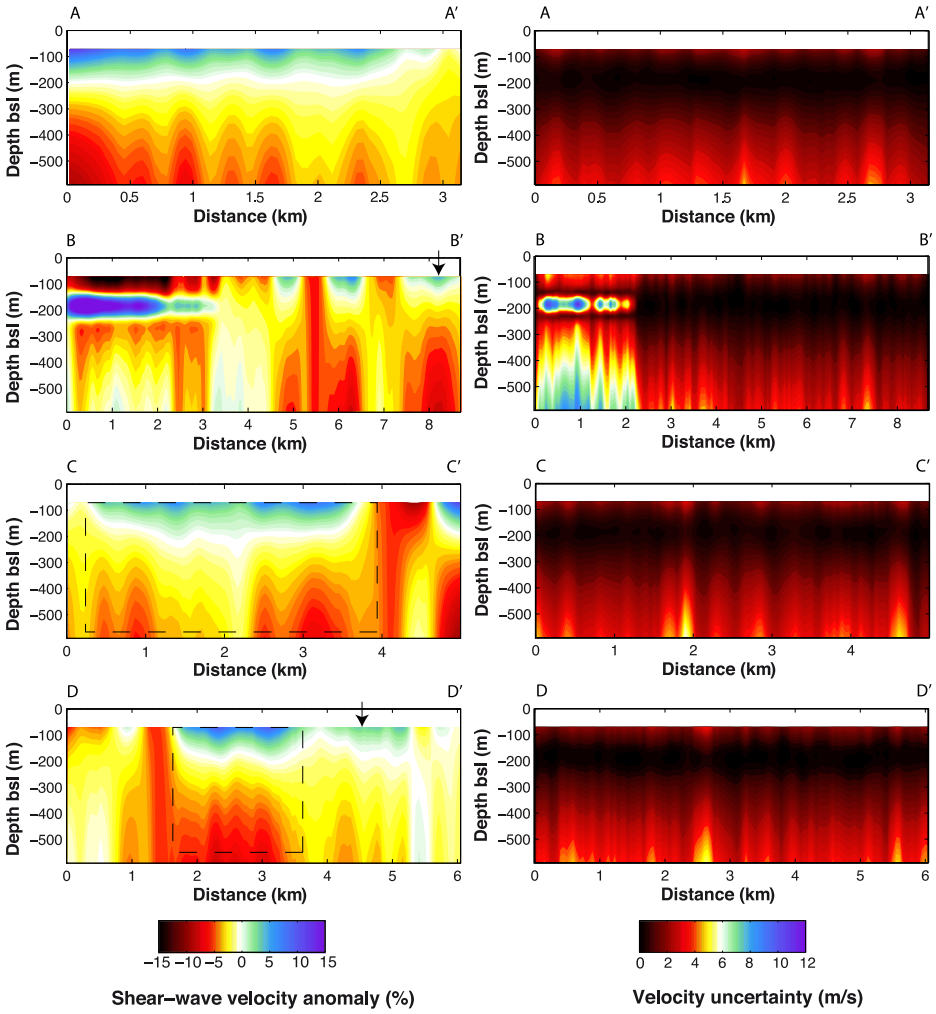

Figure 14. Left-hand panels: 2-D vertical slices across the 3-D velocity model along profiles shown in Fig. 13(d). The vertical axis has been multiplied by a factor 5. The profile AA′ is along the northern palaeochannel, the profile BB′ is along the southern palaeochannel and crosses the northern one, the profile CC′ crosses the subsidence bowl as well as the profile DD′. The dashed boxes delineate the subsidence effects. The arrows in profiles BB′ and DD′ show the positions of the northern palaeochannel. Right-hand panels: absolute velocity uncertainty obtained as the standard deviation of the 1000 best-fitting models at each location. These absolute uncertainties represents less than 5 per cent uncertainty for the velocity anomalies.

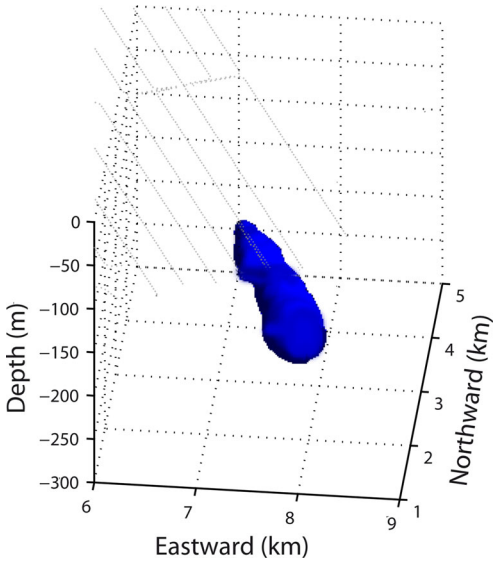

Figure 15. 3-D view of iso-contour at +15 per cent velocity anomaly showing the shape of the large palaeochannel at the south of the array.

non-unicity of the solutions. The results are, therefore, more robust showing a reasonable spatial resolution in both horizontal and vertical directions. The retrieved geological structures are well defined and are located at depths similar to those found with the FWI from an active experiment (Sirgue *et al.* 2010). The 3-D velocity cube also permits to precise the depth extent of the reservoir subsidence effects both in deeper parts (below 150 m) and at the surface with rocks compression coupled with high velocity at the surface and extension coupled with low-velocity zones near the bottom of the model. The possibility to obtain such a high-resolution model using such a short recording time paves the way to an efficient near real-time monitoring of the shallow overburden at Valhall. On the other hand, such a model could be used to precise *S*-wave statics or could also be a good candidate for a starting model used in future FWIs.

ACKNOWLEDGEMENTS

We thank Andrew Curtis and an anonymous reviewer for providing us with comments which help to improve the quality of this paper. We thank BP Norge AS and the Valhall partner, Hess Norge AS, for granting access to the seismic data. The authors also acknowledge

the use of resources provided by the European Grid Infrastructure. For more information, please consult the EGI-InSPIRE paper (http://go.egi.eu/pdnon). The contribution of AM, NS and PR was supported by a FP7 ERC Advanced grant 227507 (WHISPER). This is IPGP contribution number 3544.

REFERENCES

Aki, K., 1957. Space and time spectra of stationary stochastic waves with special reference to microtremors, *Bull. Earthq. Res. Inst.,* **35,** 415–456.

Barkved, O.I., 2012. *Seismic Surveillance for Reservoir Delivery From a Practitioner's Point of View (EET 6),* EAGE Publications bv.

Barkved, O.I., Kristiansen, T.I. & Fjær, E.I., 2005. The 4D Seismic Response of a Compacting Reservoir-Examples From the Valhall Field, Norway., in *SEG Technical Program Expanded Abstracts, Annual Meeting,* **24**(1), doi:10.1190/1.2148232.

Barmin, M.P., Ritzwoller, M.H. & Levshin, A.L., 2001. A fast and reliable method for surface wave tomography, *Pure appl. Geophys.,* **158**(8), 1351–1375.

Boué, P., Poli, P., Campillo, M., Pedersen, H., Briand, X. & Roux, P., 2013. Teleseismic correlations of ambient seismic noise for deep global imaging of the Earth, *Geophys. J. Int.,* doi:10.1093/gji/ggt160.

Brenguier, F., Shapiro, N.M., Campillo, M., Nercessian, A. & Ferrazzini, V., 2007. 3-D surface wave tomography of the Piton de la Fournaise volcano using seismic noise correlations, *Geophys. Res. Lett.,* **34**(2), 2305, doi:10.1029/2006GL028586.

Brocher, T.M., 2005. Empirical relations between elastic wavespeeds and density in the earth's crust, *Bull. seism. Soc. Am.,* **95**(6), 2081–2092.

Buckingham, M.J., 2000. Wave propagation, stress relaxation, and grain-to-grain shearing in saturated, unconsolidated marine sediments, *Acoust. Soc. Am. J.,* **108,** 2796–2815.

Buckingham, M.J., 2005. Compressional and shear wave properties of marine sediments: comparisons between theory and data, *Acoust. Soc. Am. J.,* **117,** 137–152.

Bussat, S. & Kugler, S., 2011. Offshore ambient-noise surface-wave tomography above 0.1 Hz and its applications, *Leading Edge,* **30**(5), 514, doi:10.1190/1.3589107.

Calò, M., Kinnaert, X. & Dorbath, C., 2013. Procedure to construct three-dimensional models of geothermal areas using seismic noise cross-correlations: application to the Soultz-sous-Forêts enhanced geothermal site, *Geophys. J. Int.,* **194**(3), 1893–1899.

Campillo, M., 2006. Phase and correlation in 'random' seismic fields and the reconstruction of the Green function, *Pure appl. Geophys.,* **163**(23), 475–502.

Campillo, M., Roux, P. & Shapiro, N.M., 2011. Correlation of seismic ambient noise to image and monitor the solid Earth, *Encyclopedia of Solid Earth Geophysics,* Springer-Verlag. doi:10.1007/978-90-481-8702-7.# Science+Business Media B.V.

Castagna, J.P., Batzle, M.L. & Eastwood, R.L., 1985. Relationships between compressional-wave and shear-wave velocities in clastic silicate rocks, *Geophysics,* **50**(4), 571–581.

de Ridder, S.A.L. & Biondi, B.L., 2013. Daily reservoir-scale subsurface monitoring using ambient seismic noise, *Geophys. Res. Lett.,* **40,** 2969–2974.

de Ridder, S. & Dellinger, J., 2011. Ambient seismic noise eikonal tomography for near-surface imaging at Valhall, *Leading Edge,* **30**(5), 506–512.

Ekström, G., 2011. A global model of Love and Rayleigh surface wave dispersion and anisotropy, 25-250 s, *Geophys. J. Int.,* **1,** 311, doi:10.1111/j.1365-246X.2011.05225.x.

Gabriels, P., Snieder, R. & Nolet, G., 1987. In situ measurements of shear-wave velocity in sediments with higher-mode Rayleigh waves, *Geophys. Prospect.,* **35,** 187–196.

Gouédard, P. *et al.*, 2008. Cross-correlation of random fields: mathematical approach and applications, *Geophys. Prospect.,* **56**(3), 375–393.

Halliday, D. & Curtis, A., 2008. Seismic interferometry, surface waves and source distribution, *Geophys. J. Int.,* **175**(3), 1067–1087.

Hamilton, E.L., 1976. Shear-wave velocity versus depth in marine sediments: A review, *Geophysics,* **41**(5), 985–996.

Hatchell, P.J., Wills, P.B. & Didraga, C., 2009. Production induced effects on near-surface wave velocities at Valhall, in *Proceedings of the 71st EAGE Conference and Exhibition,* SPE, EAGE.

Herbers, T.H.C. & Guza, R.T., 1994. Nonlinear wave interactions and high-frequency seafloor pressure, *J. geophys. Res.,* **99**(C5), 10 035–10 048.

Herrmann, R.B. & Ammon, C.J., 2004. *Surface waves, receiver functions and crustal structure,* Computer Programs in Seismology.

Huang, Y.-C., Yao, H., Huang, B.-S., van der Hilst, R.D., Wen, K.-L., Huang, W.-G. & Chen, C.-H., 2010. Phase velocity variation at periods of 0.5–3 seconds in the Taipei Basin of Taiwan from correlation of ambient seismic noise, *Bull. seism. Soc. Am.,* **100**(5A), 2250–2263.

Kimman, W.P. & Trampert, J., 2010. Approximations in seismic interferometry and their effects on surface waves, *Geophys. J. Int.,* **182**(1), 461–476.

Kristiansen, T. & Plischke, B., 2010. History matched full field geomechanics model of the Valhall Field including water weakening and re-pressurisation, in *Proceedings of the SPE EUROPEC/EAGE Annual Conference and Exhibition,* Barcelona, Spain.

Kustowski, B., Ekström, G. & Dziewoński, A.M., 2008. Anisotropic shear-wave velocity structure of the Earth's mantle: a global model, *J. Geophys. Res.: Solid Earth (1978–2012),* **113**(B6), doi:10.1029/2007JB005169.

Levshin, A.L., Yanovskaya, T.B., Lander, A.V., Bukchin, B.G., Barmin, M.P., Ratnikova, L.I. & Its, E.N., 1989. Seismic surface waves in a laterally inhomogeneous Earth, *Kluwer*.

Lin, F.C., Ritzwoller, M.H., Townend, J., Bannister, S. & Savage, M.K., 2007. Ambient noise Rayleigh wave tomography of New Zealand, *Geophys. J. Int.,* **170**(2), 649–666.

Lin, F.C., Moschetti, M.P. & Ritzwoller, M.H., 2008. Surface wave tomography of the western United States from ambient seismic noise: Rayleigh and Love wave phase velocity maps, *Geophys. J. Int.,* **173**(1), 281–298.

Lin, F.C., Ritzwoller, M.H. & Snieder, R., 2009. Eikonal tomography: surface wave tomography by phase front tracking across a regional broad-band seismic array, *Geophys. J. Int.,* **177**(3), 1091–1110.

Lin, F.-C., Tsai, V.C., Schmandt, B., Duputel, Z. & Zhan, Z., 2013. Extracting seismic core phases with array interferometry, *Geophys. Res. Lett.,* **40,** 1049–1053.

Longuet-Higgins, M.S., 1950. A theory of the origin of microseisms, *Phil. Trans. R. Soc. Lond., A. Math. Phys. Sci.,* **243**(857), 1–35.

Luzón, F., Almendros, J. & García-Jerez, A., 2011. Shallow structure of Deception Island, Antarctica, from correlations of ambient seismic noise on a set of dense seismic arrays, *Geophys. J. Int.,* **185**(2), 737–748.

Masterlark, T., Haney, M., Dickinson, H., Fournier, T. & Searcy, C., 2010. Rheologic and structural controls on the deformation of Okmok volcano, Alaska: FEMs, InSAR, and ambient noise tomography, *J. geophys. Res.,* **115**(B2), B02409, doi:10.1029/2009JB006324.

Mooney, W.D, Laske, G. & Masters, T.G., 1998. CRUST 5.1: A global crustal model at 5° × 5°, *J. geophys. Res.: Solid Earth (1978–2012),* **103**(B1), 727–747.

Mordret, A., Landès, M., Shapiro, N.M., Singh, S.C., Roux, P. & Barkved, O.I., 2013a. Near-surface study at the Valhall oil field from ambient noise surface wave tomography, *Geophys. J. Int.,* **193**(3), 1627–1643.

Mordret, A., Shapiro, N.M., Singh, S., Roux, P., Montagner, J.-P. & Barkved, O., 2013b. Azimuthal anisotropy at Valhall: the Helmholtz equation approach, *Geophys. Res. Lett.,* **40,** doi:10.1029/2009JB006324.

Mordret, A., Shapiro, N.M., Singh, S.C., Roux, P. & Barkved, O.I., 2013c. Helmholtz tomography of ambient noise surface wave data to estimate Scholte wave phase velocity at Valhall Life of the Field, *Geophysics,* **78**(2), WA99–WA109.

Moschetti, M.P., Ritzwoller, M.H. & Shapiro, N.M., 2007. Surface wave tomography of the western United States from ambient seismic noise: Rayleigh wave group velocity maps, *Geochem. Geophys. Geosyst.,* **8**(8), doi:10.1029/2007GC001655.

Munns, J.W., 1985. The Valhall field: a geological overview, *Mar. Petrol. Geol.,* **2**(1), 23–43.

Nishida, K., 2013. Global propagation of body waves revealed by cross-correlation analysis of seismic hum, *Geophys. Res. Lett.,* **40,** doi:10.1002/grl.50269.

Nishida, K., Montagner, J.-P. & Kawakatsu, H., 2009. Global surface wave tomography using seismic hum, *Science,* **326**(5949), 112–112.

Okada, H. & Suto, K., 2003. The Microtremor Survey Method, Vol. 12, Society of Exploration Geophysicists with the cooperation of Society of Exploration Geophysicists of Japan and Australian Society of Exploration Geophysicists.

Pollitz, F.F. & Snoke, J.A., 2010. Rayleigh-wave phase-velocity maps and three-dimensional shear velocity structure of the western US from local non-plane surface wave tomography, *Geophys. J. Int.,* **180**(3), 1153–1169.

Renalier, F., Jongmans, D., Campillo, M. & Bard, P.-Y., 2010. Shear wave velocity imaging of the Avignonet landslide (France) using ambient noise cross correlation, *J. geophys. Res.,* **115**(F3), F03032, doi:10.1029/2009JF001538.

Ritzwoller, M.H., Lin, F.C. & Shen, W., 2011. Ambient noise tomography with a large seismic array, *Comptes Rendus Geoscience,* **343**(8), 558–570.

Rodriguez-Suarez, C. & Stewart, R.R., 2000. Shear-wave velocities in shallow marine sediments, in *SEG Technical Program Expanded Abstracts 2000,* pp. 1871–1874.

Sambridge, M., 1999. Geophysical inversion with a neighbourhood algorithmI. Searching a parameter space, *Geophys. J. Int.,* **138**(2), 479–494.

Shapiro, N.M. & Ritzwoller, M.H., 2004. Thermodynamic constraints on seismic inversions, *Geophys. J. Int.,* **157**(3), 1175–1188.

Shapiro, N.M., Ritzwoller, M.H., Mareschal, J.C. & Jaupart, C., 2004. Lithospheric structure of the Canadian Shield inferred from inversion of surface-wave dispersion with thermodynamic a priori constraints, *Geol. Soc., Lond., Special Publications,* **239**(1), 175–194.

Shapiro, N.M., Campillo, M., Stehly, L. & Ritzwoller, M.H., 2005. High-resolution surface-wave tomography from ambient seismic noise, *Science,* **307**(5715), 1615, doi:10.1126/science.1108339.

Sirgue, L., Barkved, O.I., Dellinger, J., Etgen, J., Albertin, U. & Kommedal, J.H., 2010. Full waveform inversion: the next leap forward in imaging at Valhall, *First Break,* **28,** 65–70.

Stankiewicz, J., Ryberg, T., Haberland, C., Fauzi & Natawidjaja, D., 2010. Lake Toba volcano magma chamber imaged by ambient seismic noise tomography, *Geophys. Res. Lett.,* **37**(17), L17306, doi:10.1029/2010GL044211.

Stehly, L., Fry, B., Campillo, M., Shapiro, N.M., Guilbert, J., Boschi, L. & Giardini, D., 2009. Tomography of the Alpine region from observations of seismic ambient noise, *Geophys. J. Int.,* **178**(1), 338–350.

Stein, S. & Gordon, R.G., 1984. Statistical tests of additional plate boundaries from plate motion inversions, *Earth planet. Sci. Lett.,* **69**(2), 401–412.

Trampert, J. & Spetzler, J., 2006. Surface wave tomography: finite-frequency effects lost in the null space, *Geophys. J. Int.,* **164**(2), 394–400.

VanGestel, J.-P., Kommedal, J.H., Barkved, O.I., Mundal, I., Bakke, R. & Best, K.D., 2008. Continuous seismic surveillance of Valhall Field, *Leading Edge,* **27**(12), 1616–1621.

Wathelet, M., Jongmans, D. & Ohrnberger, M., 2004. Surface wave inversion using a direct search algorithm and its application to ambient vibration measurements, *Near Surf. Geophys.,* **2**(4), 211–221.

Wathelet, M., Jongmans, D. & Ohrnberger, M., 2005. Direct inversion of spatial autocorrelation curves with the neighborhood algorithm, *Bull. seism. Soc. Am.,* **95**(5), 1787–1800.

Xia, J., Miller, R.D. & Park, C.B., 1999. Estimation of near-surface shear-wave velocity by inversion of Rayleigh waves, *Geophysics,* **64**(3), 691–700.

Yang, Y., Ritzwoller, M.H., Levshin, A.L. & Shapiro, N.M., 2007. Ambient noise Rayleigh wave tomography across Europe, *Geophys. J. Int.,* **168,** 259–274.

Yang, Y., Ritzwoller, M.H., Lin, F.-C., Moschetti, M.P. & Shapiro, N.M., 2008. Structure of the crust and uppermost mantle beneath the western United States revealed by ambient noise and earthquake tomography, *J. geophys. Res.: Solid Earth (1978–2012),* **113**(B12), doi:10.1029/2008JB005833.

Yang, Y., Ritzwoller, M.H. & Jones, C.H., 2011. Crustal structure determined from ambient noise tomography near the magmatic centers of the coso region, Southeastern California, *Geochem. Geophys. Geosyst.,* **12**(2), doi:10.1029/2010GC003362.

Yao, H., Van Der Hilst, R.D. & De Hoop, M.V., 2006. Surface-wave array tomography in SE Tibet from ambient seismic noise and two-station analysis–I. Phase velocity maps, *Geophys. J. Int.,* **166**(2), 732–744.

Zheng, S., Sun, X., Song, X., Yang, Y. & Ritzwoller, M.H., 2008. Surface wave tomography of China from ambient seismic noise correlation, *Geochem. Geophys. Geosyst.,* **9**(8), doi:10.1029/2008GC001981.

Zheng, Y., Shen, W., Zhou, L., Yang, Y., Xie, Z. & Ritzwoller, M.H., 2011. Crust and uppermost mantle beneath the North China Craton, northeastern China, and the Sea of Japan from ambient noise tomography, *J. geophys. Res.: Solid Earth (1978–2012),* **116**(B12), doi:10.1029/2011JB008637.